Chapter 8
Atomic Force Microscopy of Viruses

Pedro J. de Pablo

Abstract Atomic force microscopy (AFM) is a helpful tool to acquire nanometric-resolution images, and also to perform a certain physical characterization of specimens, including their stiffness and mechanical resilience. Besides of the wide range of applications, from materials science to biology, this technique works in a variety of conditions as long as the sample is supported on a solid surface, in air, ultra high vacuum or, most importantly for virus research, in liquids. The adaptability of this technique is also fostered by the variety of sizes of the specimens that it can dealt with, such as atoms, molecules, molecular complexes including viruses and cells, and the possibility to observe dynamic processes in real time. Indeed, AFM facilitates single molecule experiments enabling not only to *see* but also to *touch* the material under study (*i.e.*, to undertake mechanical manipulations), and constitutes a fundamental source of information for material characterization. In particular, the study of the mechanical properties at the nano-scale of viruses and other biomolecular aggregates, is providing an important set of data which help to elaborate mechano-chemical structure/function models of molecular biomachines, expanding and complementing the information obtained by other structural techniques.

Keywords Atomic force microscopy • Force • Beam deflection • Tip • Cantilever • Stylus • Topography • Mechanics • Liquids • Tip-sample dilation • Adsorption • Virus • Capsid • Virion • Deformation • Nanoindentation • Force curve • Disruption • Breakage

P.J. de Pablo (✉)
Department of Physics of the Condensed Matter, C03, Facultad de Ciencias, Universidad Autónoma de Madrid, Campus de Cantoblanco, 28049 Madrid, Spain
e-mail: p.j.depablo@uam.es

M.G. Mateu (ed.), *Structure and Physics of Viruses: An Integrated Textbook*, Subcellular Biochemistry 68, DOI 10.1007/978-94-007-6552-8_8,

Abbreviations

AFM	Atomic force microscopy
CCD	Charge-coupled device
CM	Contact mode
DM	Dynamic mode
EDL	Electrostatic double layer
EM	Electron microscopy
HOPG	Highly oriented pyrolytic graphite
JM	Jumping mode
MVM	Minute virus of mice
STM	Scanning tunneling microscopy
UHV	Ultra-high vacuum

8.1 Introduction

The word *microscope* suggests an optical device that uses light to achieve a magnified image of a small object. Consequently, the question that arises when seeing an atomic force microscope (AFM) for the first time is: where do I have to look to see the object? In a conventional microscope (Fig. 8.1), a source emits particles, such as electrons or photons, that interact with the specimen. A detector registers and communicates this interaction to an analyzer, which processes the information received to make it comprehensible. Optical and electron microscopes fit into this source-specimen-detector-analyzer scheme.

In the optical microscope, the photons emitted by the incandescent lamp are conveniently manipulated by a system of lenses, both before and after the interaction with the specimen, finally arriving to the eyepiece where the detector (*i.e.* the eyes, film or charge-coupled device, CCD) collects the information. A typical optical microscope using visible light can reach a resolution of $\lambda/2 \sim 200$ nm (λ being the wavelength of the light).

In the case of electron microscopy (EM) (see Chap. 3), a filament emits electrons and a system of electromagnetic lenses are used to manipulate and focus the electron beam both before and after the interaction with the specimen. Afterwards the electrons are collected by a phosphorescent screen, film or CCD. In 1933 the German engineering Ernst Ruska constructed an electron microscope that exceeded the maximum resolution of an optical microscope, reaching about 1 nm.

AFM is not based in registering interactions between probe particles, such as photons and electrons, and the sample. In AFM the probe is a nanometric tip at the end of a microcantilever which mechanically palpates the object under study like a blind person uses a walking stick. In this way AFM enables the construction of a topographic image based upon recording the deflection angle of the microcantilever at each point of the studied sample. In this chapter, I describe the conceptual and

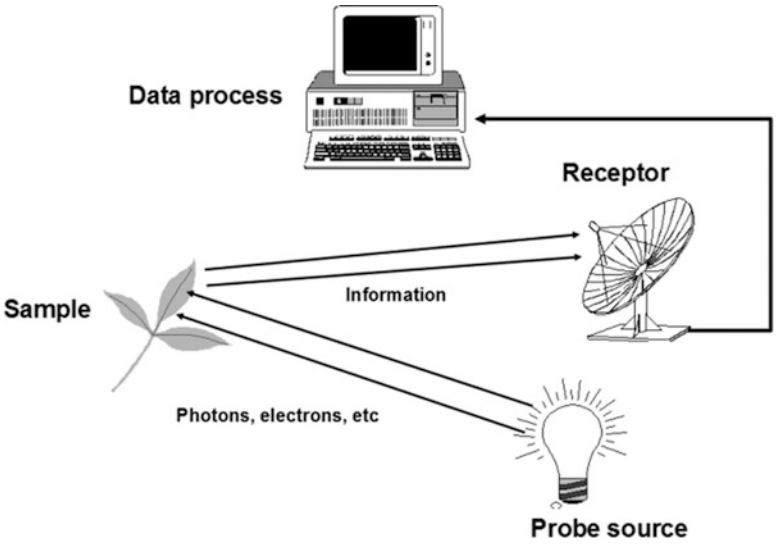

Fig. 8.1 Concept of microscopy. Any microscope requires probe source, sample, receptor and data analysis

technical bases of AFM. In particular, I refer to working methods in liquids and its applications for imaging virus particles and viral components (Fig. 8.2) In a related Chapter (Chap. 18), the application of AFM to determine the mechanical properties of virus particles is described.

8.2 Basic Concepts

In scanning probe microscopy a sharp stylus of a few nanometers in diameter, which can be considered as a probe, approaches the surface of the sample. Binnig and Rohrer [7] invented the Scanning Tunneling Microscope (STM) and received the Nobel Prize for Physics along with Ruska in 1986. The STM is based on a quantum effect (tunneling) that occurs when a sharp metallic tip is brought to a distance (z) of less than 1 nm from a conductive surface. This effect involves the flow of an electronic current (I) between the surface and the tip according to the formula $I \propto \exp(-\sqrt{\phi}z)$, where ϕ is the work-function of the metallic surface [8]. The strong dependence on the tip-surface distance can be used to obtain topographic and electronic maps of the sample by moving, (*i.e.* scanning) the tip on the surface while keeping the tip-sample distance constant through a feedback algorithm. Although this tool provides true atomic resolution in ultra-high vacuum (UHV) conditions, a mandatory requisite is that both the tip and sample should be conductive. Therefore, STM is not suitable for biological samples since these are mainly insulators, which need to be covered with a metallic layer [9].

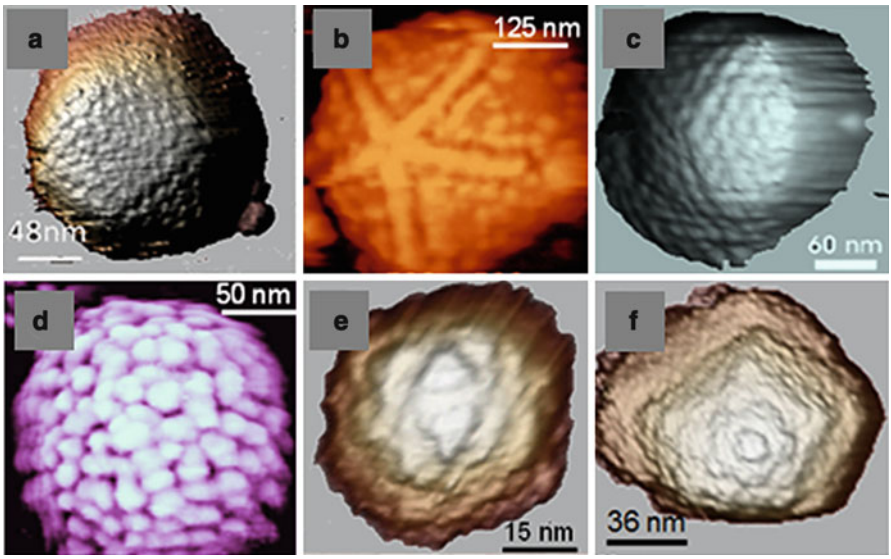

Fig. 8.2 A gallery of virus images obtained by AFM. (**a**) Human adenovirus, taken from Ref. [1]. (**b**) Giant mimivirus, taken from Ref. [2]. (**c**) Herpes simplex virus, taken from Ref. [3]. (**d**) Moloney murine leukemia virus, after taken from [4]. (**e**) MVM, taken from [5]. (**f**) bacteriophage T7, taken from [6]. All images are reproduced with permission

In 1986 Binnig, Quate and Gerber invented the AFM [10] combining the principles of both the STM and the so-called stylus profilometer [11]. In an AFM (Fig. 8.3) a sharp tip (approximately tens of nm in radius) attached to the end of a microcantilever is approached to the surface of an object by means of a piezoelectric device. As a consequence a force appears between the tip and surface that can be attractive or repulsive (see below) causing the cantilever to bend. A feedback algorithm acting on the piezoelectric device controls the relative tip-surface distance, and a topographic map of the object is obtained by scanning the surface in a plane perpendicular to the tip. The original article by Binnig et al. [10] presents the topographic profiles obtained for an insulator (ceramic). The fact that both tip and sample may be insulators is one of the main advantages of AFM, opening the door to a whole range of possibilities such as the study of biological samples including proteins, nucleic acids, membranes, cells, and biomolecular complexes such as viruses.

8.3 AFM Implementation

Although there are a variety of routes to control the deflection of the cantilever in AFM, here we will focus on the beam deflection method [12] since it is commonly employed when working with biological samples. The beam deflection system

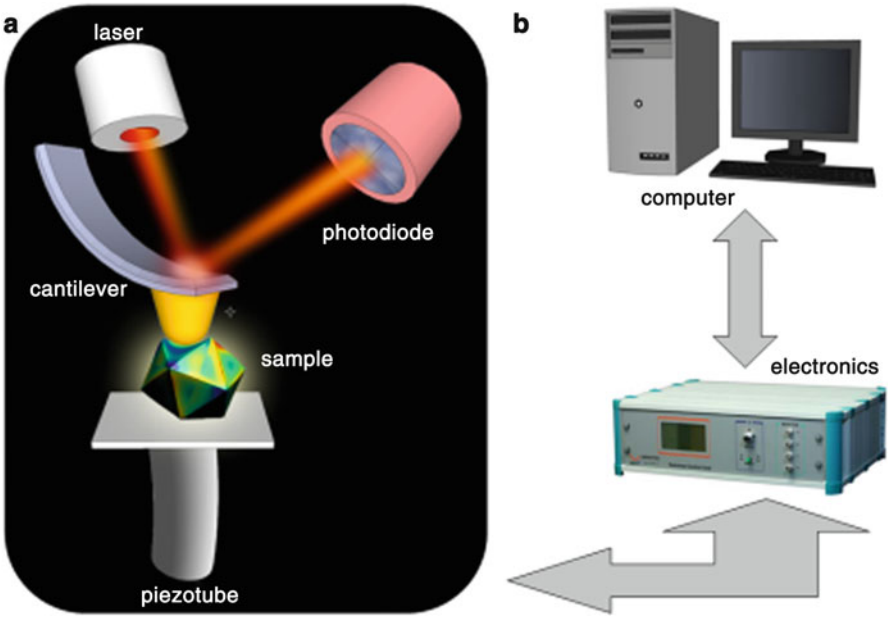

Fig. 8.3 Principle of atomic force microscopy. The software running on the computer controls the electronics (**b**), which gives and receives information to and from the AFM head (**a**)

involves focusing a laser beam on the end of the cantilever and collecting the reflected light with a photodiode (Fig. 8.3a). As a consequence, any bending of the cantilever will affect the position of the reflected laser spot on the photodiode. A normal bending will originate a so-called normal force signal, $F_{n,}$ on the photodiode sectors, whereas a lateral torsion will result in the so-called lateral force, F_l.

The core of an AFM is the head (Fig. 8.3a), where the beam deflection system is integrated along with the piezoelectric device (piezo-tube) that moves the sample in all three directions (x, y, z). In Fig. 8.3a an AFM head configuration is shown where the tip is fixed and the sample is moved by the piezo-tube. Another configuration known as "stand alone", fixes the sample and the tip makes the scanning movement controlled by a piezo-tube that carries the cantilever. The electronic components receive the signals coming from the photodiode, mainly F_n and F_l, and provide high voltages (up to hundreds of volts) to move the piezo-tube to which the sample (or cantilever) is attached. The computer is in charge for managing the data and calculating all the parameters required to move the piezo-tube in a convenient way by using the electronics (Fig. 8.3b). Details on the different components of a typical AFM and AFM operation are given in the following subsections.

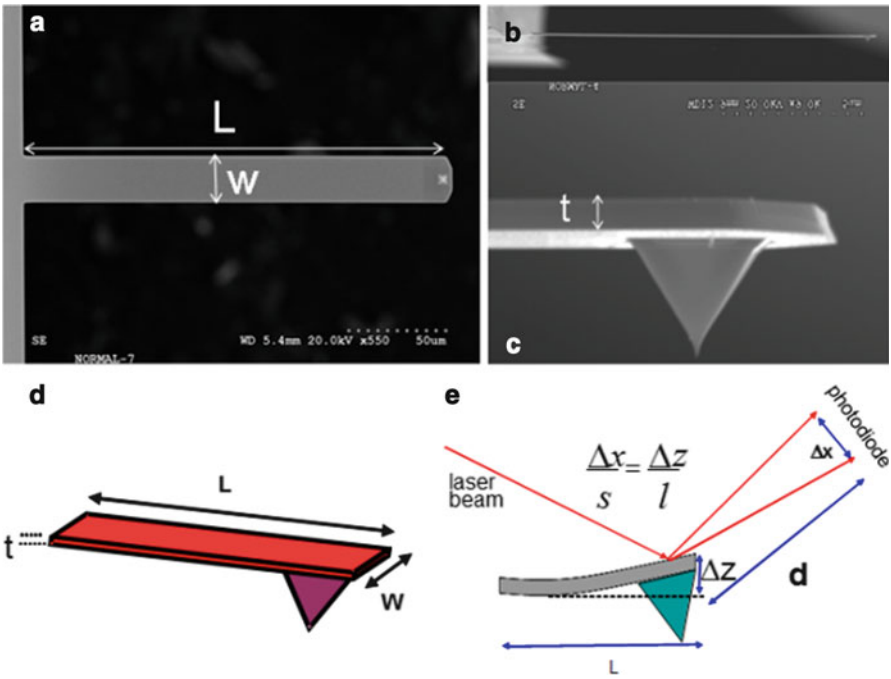

Fig. 8.4 AFM cantilevers. (**a**) and (**b**) respectively show top and side views of a rectangular cantilever of 150 μm in length (L) and 25 μm in width (w) attached to a chip. (**c**) presents a close-up image of a pyramidal tip, and a cantilever with a thickness of 150 nm. (**d**) sketches the geometry of a rectangular cantilever. The cartoon in (**e**) indicates the vertical resolution of the bending cantilever as a function of several geometric parameters

8.3.1 Cantilevers

Integrated tip and cantilever assemblies can be fabricated from silicon or silicon nitride using photolithographic techniques. More than 1,000 tip and cantilever assemblies can be produced on a single silicon wafer. The cantilevers can be rectangular (Fig. 8.4a) or V-shaped, and they typically range from 60 to 200 μm in length, 10–40 μm in width, and 0.3–2 μm in thickness. The usual tip radius is about 20 nm although lower diameters can be obtained (Fig. 8.4b). The mechanical stiffness of the cantilever (see Chap. 18) is given by its spring constant k, which normally ranges between 0.03 N/m and 40 N/m, and strongly depends on the cantilever's dimensions. For example, for a rectangular cantilever $k = \frac{EW}{4}\left(\frac{t}{L}\right)^3$, where E is the Young Modulus (a measurement of the intrinsic elasticity of a solid material, see Chap. 18) of the cantilever, and W, t and L are the cantilever width, thickness and length respectively (Fig. 8.4d). While W and L can be fairly precisely known, t is always difficult to measure. As a consequence, the manufacturers normally provide the cantilever spring constant with an error of 10–30 % and therefore the user should calibrate each cantilever [13]. The spring constant k is

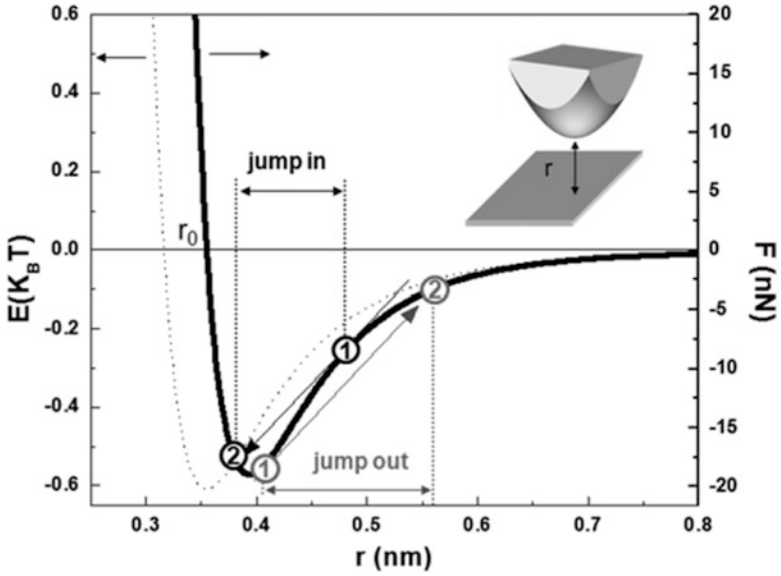

Fig. 8.5 Tip-surface interaction. *The dotted line* represents a Lennard-Jones potential as a function of the distance between atoms, r, mimicking the tip-surface interaction (represented in the *inset*). The *solid line* is the interaction force obtained from the potential. The numbers *inside the circles* indicate the cantilever instabilities (see text for a complete description)

used to calculate the force applied on the cantilever as a function of bending Δz using Hooke's law, *i.e.*, $F = k \times \Delta z$ (Fig. 8.4e).

The vertical resolution of the cantilever, Δz, strongly depends on the noise of the photodiode, since it defines the minimum significant displacement Δx, on the detector (Fig. 8.4e). A typical cantilever of 100 μm length has about 0.1 Å resolution assuming a signal-to-noise ratio around 1 [13].

Another important parameter that can have influence on the vertical resolution is the thermal noise [14]: the cantilever oscillates at the resonance frequency with an amplitude $\Delta z = \sqrt{\frac{k_B T}{k}}$, where k_B is the Boltzman constant, T is the absolute temperature and k the cantilever spring constant. For example, at room temperature, there is a noise of about 5 Å for a cantilever of spring constant 0.02 N/m.

8.3.2 Interaction Between the AFM-Tip and the Sample Surface

In order to understand the interaction between tip and sample we shall refer to potentials rather than forces. Physicists prefer this approach as potentials are scalar and therefore easier to deal with compared to vectors such as forces. For this purpose let us graphically depict the Lennard-Jones potential in Jules (J) between two atoms separated by r meters (m) in vacuum [15] (dotted curve in Fig. 8.5).

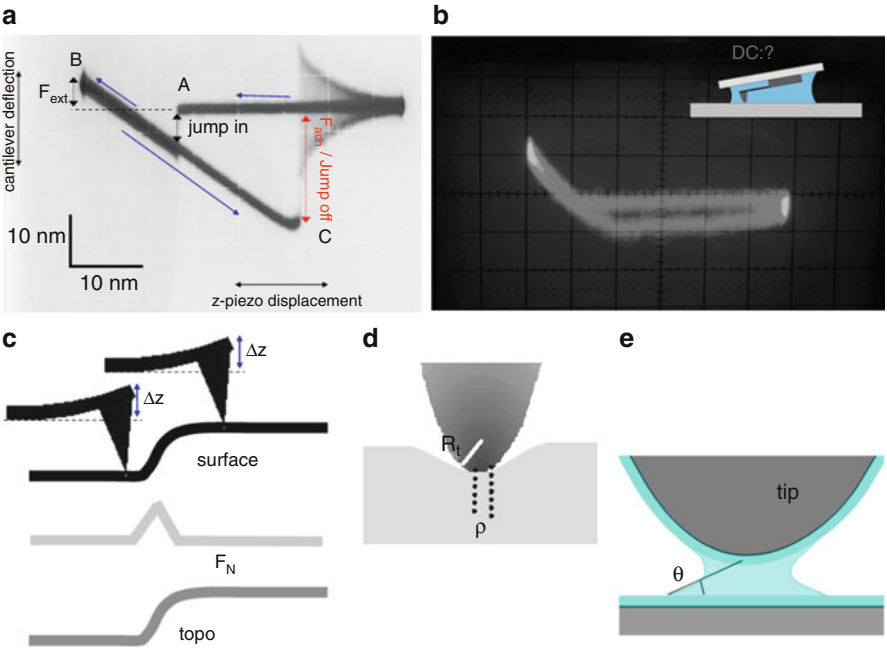

Fig. 8.6 Force vs. distance experiments, feedback and lateral resolution. (**a**) and (**b**) show oscilloscope snapshots of force vs. *z*-piezo displacement curves in air and water, respectively. (**c**) presents the contact mode showing the variation of F_n (*light gray*), and *z*-piezo tube voltage (topography, *dark gray*) as a function of a step (*black*). In (**d**) the geometric features of the tip-surface contact are depicted. (**e**) shows a cartoon illustrating the capillary forces between tip and surface (see text for a complete description)

$U(r) = -A/r^6 + B/r^{12}$, where r is the tip-sample distance, $A = 10^{-77}\ J\ m^6$ and $B = 10^{-134}\ J\ m^{12}$.

A rough approximation to the AFM tip-sample interaction is to consider the approach of two such atoms where, as depicted in the inset in Fig. 8.5: the lower part shows a solid surface and the upper part shows the apex of a sharp tip is moving downwards. An interaction force $F(r) = -\frac{dU}{dr}$ will occur and it can be seen that this force is attractive ($F < 0$) when $r > r_0$ or repulsive ($F > 0$) when $r < r_0$, (solid line curve in Fig. 8.5). These regions define the attractive and the repulsive regimes of operation, respectively.

Now let us consider the role of these regimes in a force vs. distance (FZ) AFM experiment that involves the tip approaching to the surface (Figs. 8.5 and 8.6). The experiment starts with the tip situated far from the surface in the attractive regime. As the tip is approaching and as soon as the gradient (*i.e.*, the slope) of the force equals the cantilever spring constant, the tip jumps to the surface from black point 1 to black point 2 in Fig. 8.5 (both connected by the slope). This effect is seen in the FZ of Fig. 8.6a at point A like a sudden jump of the cantilever deflection (vertical scale). In this way the tip establishes mechanical contact with the surface and it rapidly enters the repulsive regime ($F_N > 0$). The *z*-piezo (horizontal scale) is

elongated until a given F_N or deflection value is reached and then stops (point B in Fig. 8.6a). The external loading force F_{ext} can be calculated as the difference between the zero deflection position (*i.e.* before the jump to contact in point A in Fig. 8.6a) and the deflection at point B in Fig. 8.6a. Since the vertical scale is about 10 nm per division and the cantilever spring constant $k = 0.1\ N/m$ we have $F_{ext} \sim 0.5div \times 10nm/div \times 0.1nN/nm = 0.5nN$.

Subsequently, the *z*-piezo retrace cycle starts, and the tip is released from the surface at point C in Fig. 8.6a (*i.e.*, once more where the derivative of the tip-surface force equals the cantilever spring constant) jumping from the grey point 1 to grey point 2 in Fig. 8.5, following the grey arrow. The cantilever deflection jumps-off to zero with a dampened oscillation. This jump-off is known as the adhesion force F_{adh} (in Fig. 8.6a $F_{adh} \sim 2div \times 10\ nm/div \times 0.1nN/nm = 2\ nN$). The total force at point B in Fig. 8.6a is the sum of F_{ext} and F_{adh}, (*i.e.*, 2.5 *nN*). It is interesting to stress that no matter how small F_{ext} is, the total force applied to the surface will always be at least F_{adh}.

8.3.3 Contact Mode (CM)

CM is the simplest operational method used for AFM and it was the first to be developed [10]. Here the tip is brought into contact with the surface until a given deflection in the cantilever (F_n) is reached; the tip then scans a square area of the surface to obtain a topographic map. By elongating or retracting the *z*-piezo, the feedback algorithm tries to maintain the cantilever deflection constant by comparing the F_n signal with a set point reference value established by the user. Topographic data are obtained by recording the *z*-piezo voltage that the feedback algorithm is applying to correct the cantilever deflection at each position on the surface. Since the *z*-piezo is calibrated, voltages are transformed into heights and a topographic map is obtained. Let us consider a simple example where the tip is scanning a step (black line in Fig. 8.6c) with $F_n = k \times \Delta z$. When the cantilever moves to the upper part of the step, it undergoes a deflection greater than Δz. Therefore the feedback algorithm retracts the z-piezo in order to achieve the same deflection Δz as when the tip was in the lower part of the step and, as a consequence, a topographic profile of the step is obtained (blue line in Fig. 8.6c). On the other hand F_n varies at the step that is corrected by the feedback, which can be observed as a peak in the deflection signal (red line in Fig. 8.6c). The latter is known as the constant deflection mode or constant height mode, since the *z*-piezo elongation is not modified and a map of the changes in F_n is obtained. The reader is encouraged to reproduce the profiles of Fig. 8.6c when the tip goes down the step.

Let us consider now the lateral resolution that can be achieved in contact mode. We can make an estimate of this parameter by applying the Hertz theory [16], which accounts for the deformation of solids in contact. Once the tip is in contact with the sample, the radius ρ of the tip-surface contact area is given by (Fig. 8.6d):

$$\rho = \left(\frac{3 \cdot F \cdot R}{4 \cdot E^*}\right)^{1/3}$$

Where F is the applied force *i.e.* F_n; E^* is the effective Young modulus expressed by

$$\frac{1}{E^*} = \frac{1-\nu_t^2}{E_t} + \frac{1-\nu_s^2}{E_s}$$

With E_t, ν_t and E_s, ν_s being the Young Modulus and Poisson ratio for the tip and sample respectively. R is the effective radius expressed as a combination of the tip R_t and sample radius R_s,

$$\frac{1}{R} = \frac{1}{R_{tip}} + \frac{1}{R_{sample}}$$

It is worth to stress that the main condition for Hertz model applicability is that the radius of contact ρ has to be much less than the effective radius R: ρ<<R. This approximation roughly implies that the deformation is smaller than the dimensions of the tip-sample system [16]. It is important to recall that this assumption does not limit Hertz model to deformations of flat samples. In the case of metals $E = 100\ GPa$, $\nu \sim 0.5$ and the mechanical thermal noise of the cantilever is 10 pN, with $R_t \sim 20\ nm$, the radius of contact ρ is about 0.15 nm, which implies atomic resolution. However, the adhesion force in air (see below) is about 5 nN, increasing ρ to about 1 nm. Atomic resolution can be achieved by either working in liquids [17] or in UHV conditions [18], where even individual atoms can be chemically identified [19].

CM is not very frequently used to image isolated biological materials such as virus particles. The very high lateral forces that are applied to the surface [20], which can damage the sample, present an important problem when using this mode. This is especially important for single mechanically delicate biomolecules adsorbed onto a surface.

8.3.4 Dynamic Modes (DM)

In DM operation [21] the cantilever is oscillated near to or at its resonance frequency ($\omega_0 \propto \sqrt{E}t/L^2$ for a rectangular cantilever). As the tip approaches the sample the oscillating amplitude decreases until it establishes contact with the sample (Fig. 8.7a), following a similar cycle to that in Fig. 8.6a but now with oscillation. Therefore the feedback loop involves the amplitude rather than the F_n and, by keeping the oscillation amplitude constant, a topographical map of

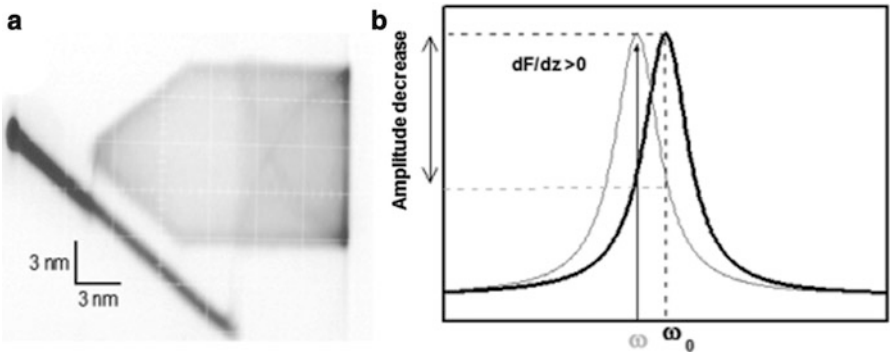

Fig. 8.7 Dynamic modes. (**a**) depicts the force vs. Piezo-tube z displacement curve of an oscillating cantilever. (**b**) illustrates the reduction of the resonance frequency of the cantilever from ω_0 to ω as the tip approaches to the surface (see text)

the object can be obtained. The amplitude is reduced because the resonance frequency (ω) changes with the tip-sample distance (z) and with the tip-sample interaction force F_{ts} according to $\frac{\Delta\omega}{\omega_0} \propto \left(\frac{1}{2k}\right)\frac{dF_{ts}}{dr}$ [22], thereby decreasing with attractive forces. The new resonance frequency ω, is lower than ω_0 and, since the cantilever is still oscillating at ω_0, the cantilever amplitude decreases (Fig. 8.7b).

While CM can damage isolated biological samples on surfaces, DM operated in non-contact mode [22] does not apply high dragging forces and is commonly used to image weakly attached molecules, including delicate biomolecules, in air. In addition to topographic maps, DM can be used to obtain other information on the sample, including a phase map (the time difference between the excitation and the response of the cantilever measured for each point in the sample), which in air carries information on the different materials composing of the sample [22].

When DM is used in liquid the situation changes completely, as the viscosity of water reduces the resonance frequency about fourfold and the quality factor (a measure of the cantilever damping) of the oscillation is reduced from ~100 to 10. When oscillating the cantilever in liquid a mechanical contact between tip and sample is established, thereby applying lateral and normal forces that may damage the specimen, especially when delicate biological objects are imaged [23]. Thus, while DM can be advantageously used to image virus particles in air, its use to image them in more physiological (liquid) conditions may be limited, unless fixation agents such as glutaraldehyde are used [24].

8.3.5 Jumping Mode (JM) or Pulse Force Mode

JM, also called pulse force mode [25, 26] is a variation of CM where lateral tip displacement occurs when the tip and sample are not in mechanical contact, thereby avoiding to a large extent shear forces and the corresponding damage to the

tip-sample system. JM performs a FZ curve (Fig. 8.6a) at every point of the sample (pixel in the image), moving the tip to the next point at the end of each cycle when the tip and sample loose contact. Feedback is engaged at point B in Fig. 8.6a, moving the piezo-tube along the z-axis in a convenient way to maintain a constant deflection or loading force F_{ext}.

JM routinely produces adhesion force maps, which provides compositional or geometrical information of the surface [27]. The adhesion force between the tip and the surface can be described as $F_{adh} = 4\pi R\gamma_L \cos\theta + 1.5\pi\Delta\gamma R$, where γ_L is the water surface tension and θ the angle of the water meniscus present between the tip and surface; R is the effective radius (described above) and $\Delta\gamma$ the tip-surface energy difference. Since the first term accounts for the water meniscus between tip and surface (Fig. 8.6e), it mainly informs about the hydrophobicity of the sample. A rough estimation of adhesion force in air at room temperature results in ~7 nN for a tip radius of about 20 nm. The second term depends mainly on the tip-surface geometry. We denote the importance of the first term by comparing the FZ curves taken from glass in both air (Fig. 8.6a) and water (Fig. 8.6b): in liquid the adhesion force is almost absent, since there is not water meniscus between the tip and sample, although some hysteresis appears in the FZ due to the dragging of the water on the cantilever. In our view, JM is a mode of choice for analyzing virus particles in liquid in close to physiological conditions, because it minimizes lateral forces and enables a precise control of the force applied [28].

8.3.6 Tip-Sample Geometrical Dilation

All of the operational modes described above give rise to an effect which is inherent to the very nature of the AFM approach: the so-called tip-sample geometrical dilation. Because of this geometry-based effect, the topography of an object in an AFM image appears as laterally expanded (see Fig. 8.8). AFM users must understand and control this artefact as much as possible in order to preclude any misunderstanding of the data obtained.

When surface asperities are of dimensions comparable to the tip radius, which is very common with many samples imaged by AFM, including virus particles, the size of the tip plays an important role on image definition and the apparent image lateral expansion due to the dilation of certain features of the image by the finite tip size [29]. Figure 8.8a, b present AFM images of single-walled carbon nanotubes on silicon oxide; these images were obtained using tips of different radii, lower in Fig. 8.8a and higher in Fig. 8.8b. A carbon nanotube is rolled-up graphene in the form of a cylinder of a few nanometers in diameter. Fig. 8.8c shows the geometric dilation effects with the different tip radii: a single topography scan line across a carbon nanotube results wider for Fig. 8.8b (black) than for Fig. 8.8a (red). This effect can be seen to arise from the geometrical considerations shown in Fig. 8.8d, and the tip radius r_t can be calculated as $r_t = b^2/2h$, where b and h are

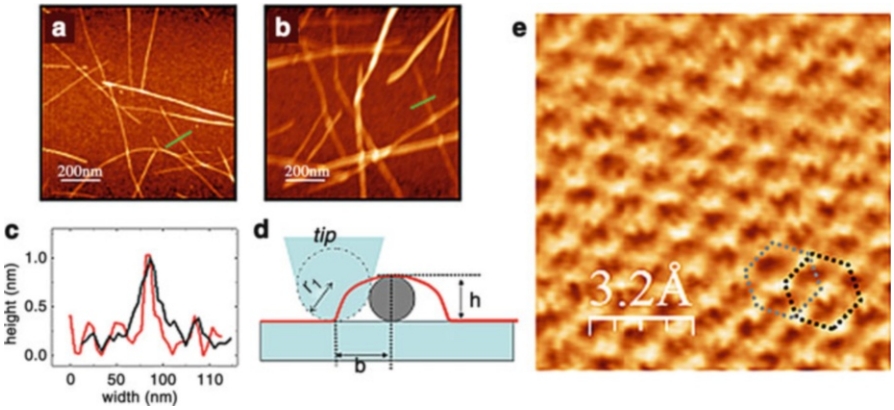

Fig. 8.8 Tip-sample dilation and atomic corrugation in HOPG. (**a**) and (**b**) show AFM images of the same samples of carbon nanotubes on silicon oxide. The topographic profiles obtained along the *green lines* in (**a**) and (**b**) show different widths due to dilation in (**c**). (**d**) illustrates the geometric parameters in the dilation process. The *red line* depicts the dilated section of the carbon nanotube section (*grey circle*). (**e**) presents the atomic corrugation of HOPG, where the two carbon layers results in two hexagonal networks

the width and the height of the sample, respectively. By using this formula, it can be calculated that the topographies of Fig. 8.8a, b have been obtained using tips with a radius of 15 nm or 70 nm, respectively. We can conclude that the sharper the tip, the better the image (which will become less laterally expanded and more defined). A popular and impressive experiment frequently used to teach AFM is to image highly oriented pyrolitic graphite (HOPG) in air [30], where the elastic deformation of the tip-sample contact plus the dilation effects result in atomic corrugation (Fig. 8.8e), although atomic defects are not visualized [31]. During imaging by AFM of virus particles and other biomolecular complexes, the height of the object at each defined point can be determined with subnanometer precision; however, the tip-sample dilation effects are important when considering lateral image dimensions and the object fine details.

8.4 Imaging Viruses and Other Biological Objects

8.4.1 Nucleic Acids, Proteins and Biomolecular Complexes

During the virus life cycle, many interactions between viral components and between viral and cellular components occur. We will review here some applications of AFM for imaging biological molecules, biomolecular complexes and their interactions.

AFM imaging in biology can be carried out in air or in liquid. Some relevant examples of AFM imaging of biomolecules in air are described first. For example, DM is frequently used for imaging DNA on a mica surface. As both DNA and mica are negatively charged, $MgCl_2$ is added to the DNA solution; the Mg^{2+} ions are sandwiched between DNA and mica, resulting in the adsorption of DNA molecules on the surface. Subsequently, the sample is dried out and DM is used to image the DNA molecules on the surface. Some structural and physical aspects of the DNA molecule have been the focus of much research using AFM [32]; in addition, an important biological application of AFM is to investigate the binding of proteins to DNA [33–35]. In this kind of single-molecule experiments the researcher is not probing the average result of the bulk reaction, but rather the action of single protein molecules on a single DNA molecule. Once the protein solution is pipetted into the DNA solution, the reaction starts and the DNA-protein complex is adsorbed onto the mica at the appropriate time and air-dried. Therefore, on the surface there is a snapshot of the process taking place between proteins and DNA, and the topography provides single molecule information of the protein-DNA complex.

However, in biology we are particularly interested in imaging in a liquid milieu in close to physiological conditions. This is an important point since biomolecules are normally fully functional only in aqueous solutions. In such a case, several particular aspects should be considered. First, a strong enough attachment of the biomolecule to the supporting surface is required to achieve good resolution during the AFM imaging process in liquid. Although biomolecules can be covalently linked to a chemically modified surface [36], covalent modifications could potentially damage the biomolecules, and therefore this treatment tends to be avoided. Fortunately, physisorption is usually sufficient and thus, the specimens can be directly adsorbed to a solid surface in a physiological buffer. The relevant forces that drive the physisorption process are the van der Waals force, the electrostatic double-layer force (EDL force) and the hydrophobic effect [37]. Unlike the van der Waals interaction, the EDL force depends strongly on the concentration and valence of charged solutes, as well as the surface charge density of both surface and specimen. The EDL force between two equally charged surfaces is repulsive and hence opposite to the van der Waals attraction [38]. One of the most extended AFM applications is to image 2-dimensional protein crystals in liquid, as well as lipid membranes, by using contact mode. Biological macromolecules become attached to the surface (mica, silicon, gold, glass, etc.) when there is a net attractive force between them and the surface pulling their surfaces into contact. This force per unit of surface (pressure) can be estimated to the light of the DLVO theory [15] like the sum of the electrostatic force between surface and molecule F_{el}, and the van der Waals interaction F_{vdW}.

$$F_{DLVO} = F_{el}(z) + F_{vdW}(z) = \frac{2\sigma_{surf}\sigma_{sample}}{\varepsilon_e \varepsilon_0} e^{-z/\lambda_D} - \frac{H_a}{6\pi z^3}$$

where z is the distance between the surface and specimen; σ_{surf} and σ_{sample} are the charge densities of surface and specimen, respectively; ε_e is the dielectric constant

of the electrolyte; ε_0 is the permittivity of vacuum; λ_D is the Debye length, that depends on the electrolyte valence [37]; and H_a the Hamaker constant. The adsorption of a sample onto freshly cleaved mica (atomically flat) can be manipulated by adjusting both the ion content and the pH of the buffer solution.

AFM in liquid is being increasingly used in molecular and cell biology [39–44]. A major application is to produce topographic images of single biomolecules and, especially, larger biomolecular complexes, lipid membranes and their embedded proteins, and whole cells in close to physiological conditions. Furthermore, by introducing variations in the conditions (*i.e.*, pH changes, addition of other biological molecules, etc.) the resulting changes in the general surface structure of the biomolecule or biological object of interest can be identified. Interestingly, in this kind of set-up the cantilever can be used also to apply forces that trigger conformational changes in single proteins molecules such as in the chaperonine GroEL; the changes thus induced may mimic those that occur under the action of physiological agents and can be revealed in real-time by AFM imaging [45].

AFM is being used also to visualize single proteins doing mechanochemical work. DM in liquid is generally used for this purpose since it is faster [46]. Maximum peak forces of a few nN are applied [23], in relation to the stiffness of the sample [47], and, although these forces could in principle be damaging to the sample, they are applied for very short periods of time such as 10 % of an oscillating period (*i.e.* for cantilever with a resonance frequency of 10 kHz in liquid, the forces are applied during 10 μs every 0.1 ms). Using this method, it has been possible to visualize, for example, the activity of RNA polymerase on DNA [48] or the conformational changes in a DNA-repair complex upon binding DNA [49]. Further high speed AFM developments have enabled to monitor the activity of single molecular machines in real-time [50].

In addition to imaging, AFM is also being applied in biology to measure the forces that participate in interactions between and within single biomolecules. AFM and optical tweezers (see Chap. 9) are major single-molecule techniques contributing to a better physics-based understanding of protein folding and unfolding, protein-ligand recognition, macromolecular assembly and disassembly, cell adhesion, etc. (*e.g.*, see references [32–35, 39–44, 46].

8.4.2 Virus Particles

Structural and chemico-physical characterization has been critical to understand the biology of viruses. X-ray crystallography (Chap. 4) and EM (cryo-EM) (Chap. 3) techniques have traditionally been used and provide direct three-dimensional structural information on whole virus particles, allowing both the interior and the surface of the virus to be visualized at high resolution. However, a limitation of these techniques is that they are both averaging ("bulk") techniques and thus they present an average time and space model of the entire population of particles in the crystal or of the many particles selected for cryo-EM image averaging. As such, these

techniques generally provide limited information on possible structural differences between individual particles in the population that distinguish them from the average structure. For this reason, the beautifully symmetrical and apparently perfect models of larger viruses derived from these techniques may be somewhat deceptive, as they may not be entirely representative of the individual viruses. Therefore, the imaging of individual virus particles may provide unique insights on the structural biology of viruses and should be considered as an important part of virus characterization [51]. In addition, AFM allows imaging viruses in liquid state and following in real-time the structural changes of individual virus particles in response to different conditions and added agents, provided the changes are not too fast (see also Sect. 6). This may enable the analysis, for example, of the stages of virus assembly or disassembly [52]. Virus particles can be disrupted upon indentations above the rupture strength [3, 53, 54], and mechanical fatigue below the rupture can be used to monitor in real time the intermediate stages of adenovirus disassembly [1]. Moreover, AFM can be used to determine some physical properties of virus particles including mechanical features (see Chap. 18). Finally, AFM enables to image and quantitate the interactions of single virus particles with other molecules and even host cells [55].

Since individual virus particles adsorb weakly to typical surfaces, they are prone to undesired modifications by lateral forces in CM or DM operation, as they are not held by a surrounding neighbourhood, unlike a protein in a 2-dimensional crystal. The typical approach for surpassing this limitation is the use of structural fixation agents, such as glutaraldehyde. In such conditions AFM may provide images whose resolution is comparable to that of some EM images [56], although still far less than that of the best structural models of virus particles recently obtained by cryo-EM (see Chap. 3). Nevertheless, since glutaraldheyde structurally reinforces the specimens subjected to study [57, 58], it precludes any characterization of processes or properties of intact native viruses, such as disassembly or mechanical features [59].

Chemical fixation is, however, not required in many instances to obtain good images or probe mechanical properties of viruses. The adsorption of viruses on solid surfaces is based on the same principles than those involved in the adsorption of DNA and proteins (Sect. 8.4.1). Although the typical approach implies the convenient sylanization of glass surfaces [60], treated mica [61] and Highly Oriented Pyrolitic Graphite (HOPG) (21) have also proved as adequate substrates for virus attachment.

In general, JM has been the preferred mode to analyze unfixed viruses, since the loading forces can be accurately controlled and lateral forces are minimized. Firstly, let us exemplify the tip-virus geometrical dilation with a prolate icosahedral virus. Figure 8.9a shows a topographic image of a bacteriophage ϕ29 virion. Its comparison with the EM model [62] is shown in Fig. 8.9b: AFM enables a reasonable structural delineation of the viral head, the neck region and the tail. When the tip-sample geometrical algorithm [29] implemented in the WSxM software [63] is applied, one observes (Fig. 8.9b) how the EM model (light contour) is dilated to the black contour in the AFM image (see Sect. 3.6). Figure 8.9c demonstrates how the geometrical dilation of the image of a ϕ29 virion adsorbed

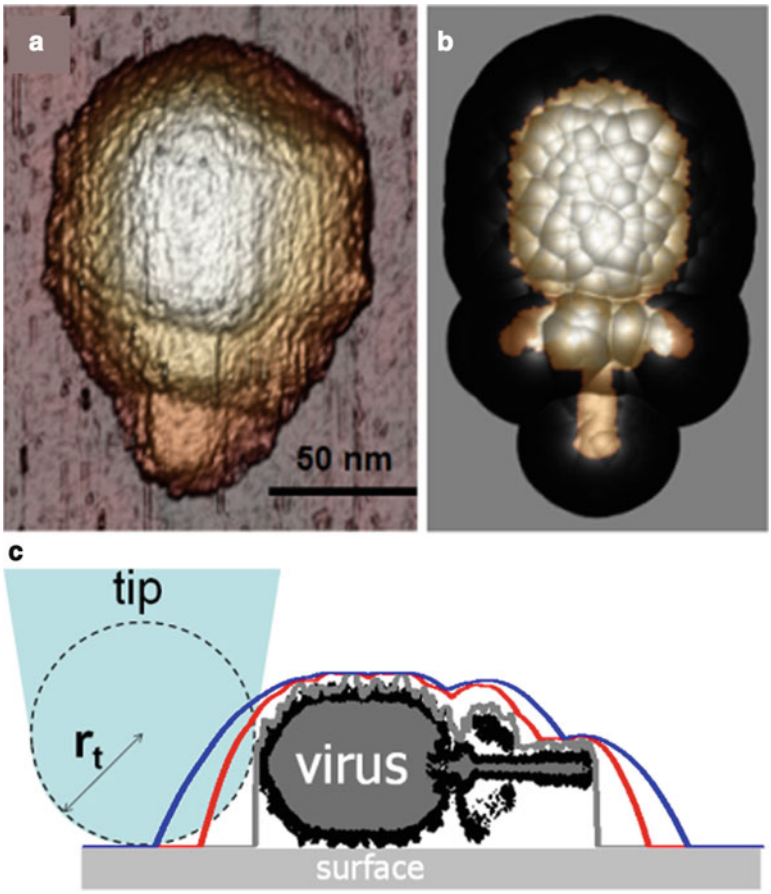

Fig. 8.9 Dilation effects in bacteriophage ϕ29 AFM images. (**a**) shows the topography of a single phage ϕ29 particle. The *bright color* image in (**b**) represents a EM structural model of ϕ29, and the *black area* indicates the dilation effects corresponding to a tip of 10 nm in diameter. The *cartoon* in (**c**) indicates the dilation effect as a function of the tip size

on a surface increases with the tip radius. A 0.5 nm-radius tip produces the grey color profile, which accurately follows the virus shape. In turn, tips of 5 and 10 nm in radius (red and blue lines, respectively) show an evident dilation and also blurring of the structural details in the virion image.

In the following, let us consider some geometrical aspects of the adsorption of icosahedral viruses (see Chap. 2) to a solid surface. For instance, the roughly spherical minute virus of mice (MVM) has a capsid of icosahedral symmetry with conspicuous protrusions at the threefold symmetry axes. Single MVM particles adsorb to the solid surface in different orientations, which frequently leaves a threefold, twofold or fivefold symmetry axis close to the top of the particle (see Figs. 8.10a–c, respectively). The possibility to identify the orientation of single

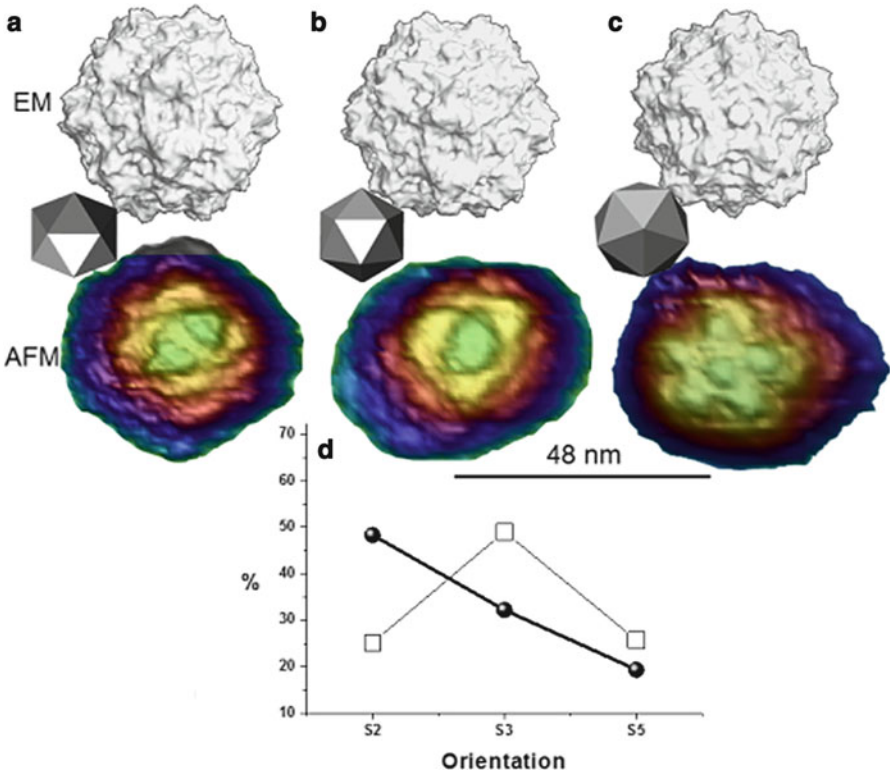

Fig. 8.10 AFM imaging of MVM. (**a**), (**b**) and (**c**) show the topographies corresponding to single MVM particles oriented with a twofold, threefold or fivefold symmetry axis on top, respectively. (**d**) represents the percentage of adsorption of each symmetry axis (*squares*) and the theoretical expectations if the adsorption through edges, faces and vertices of a perfect icosahedron were equiprobable

virus particles by resolving protrusions or other structural details allows not only a rather detailed characterization of their topography, but also the determination of local physical properties. For example, by making nanoindentations on single MVM particles adsorbed in different orientations and obtaining FZ curves, it has been shown that the viral single-stranded DNA genome is responsible for an anisotropic mechanical stiffening the virion relative to the DNA-free capsid [64], something that could be important for preserving viral infectivity. Moreover, it was possible to selectively disrupt these DNA-protein interactions or replace amino acid residues in selected regions of the MVM capsid and thereby engineer virus particles with altered mechanical properties [5] (see Chap. 18). Human adenovirus represents another example in which the orientation of single particles imaged by AFM could be determined on the adsorption of icosahedral viruses on a surface (Fig. 8.11). In this case, viruses attach to mica previously treated with $NiCl_2$ [28]. Comparison among

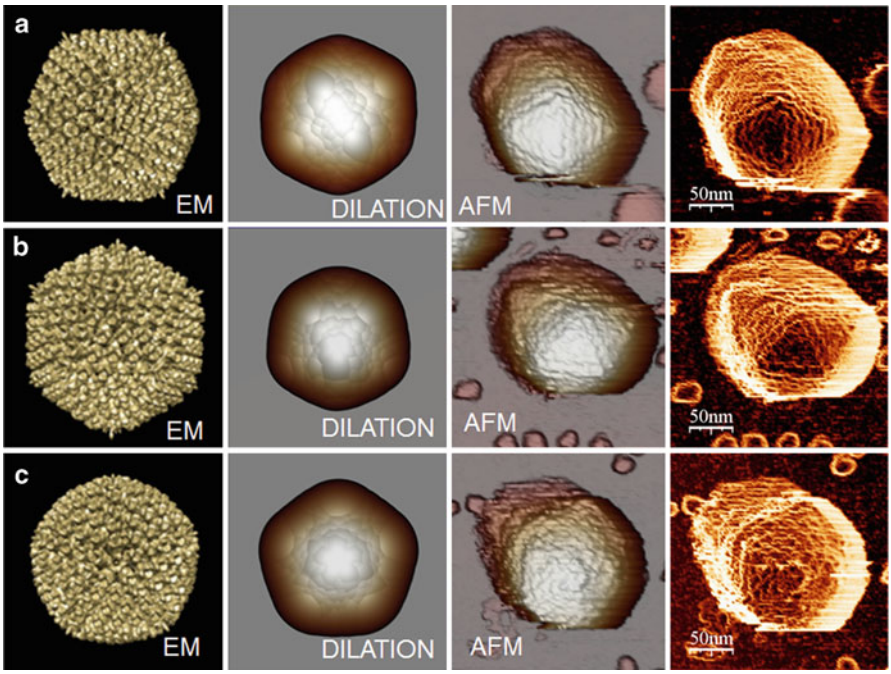

Fig. 8.11 AFM imaging of human adenovirus. (**a**), (**b**) and (**c**) show the topographies corresponding to single adenovirus particles oriented with a twofold, threefold or fivefold symmetry axis on top, respectively. AFM images are compared with EM and EM dilated structural models. The *right column* shows AFM topographic images that have been filtered to enhance the borders by obtaining the cosine of the angle between the normal vector of the surface and the normal direction of the paper sheet

EM data, EM geometrically dilated images and AFM images enabled a rapid identification of the particle orientation (see Figs. 8.11a–c for particles oriented along a twofold, threefold or fivefold symmetry axis, respectively).

It may be instructive to quantify the adsorption geometries found in MVM particles (Fig. 8.10d). Black circles represent the orientation likelihood of an icosahedron on a surface provided that the adsorption through vertices (fivefold symmetry), edges (twofold symmetry) and faces (threefold symmetry) is equally probable. If such were the case, a twofold symmetry orientation would exhibit the highest adsorption probability because in an icosahedron there are more edges (30) than faces (20) and vertices (12). On the other hand, empty squares depict the experimental results, which prime the threefold symmetry axis adsorption with almost a 50 % of the adsorbed particles. Since the threefold orientation maximizes the icosahedron area of contact, in contrast with edges or vertices, the particle-surface adsorption forces may depend strongly on the virus-surface contact area (Fig. 8.10d).

8.5 Understanding Viruses: Some Major Contributions of AFM

AFM enables new possibilities for studying virus particles, complementing classic structural approaches such as EM and X-ray crystallography. First, AFM may routinely work with individual viral particles. Second, they can be studied in liquid phase, in conditions which are closer to the *in vivo* environment. Although the resolution of AFM images is not comparable to that of structural models obtained by cryo-EM or X-ray crystallography, AFM enables the identification of virus elements which are not symmetrically ordered. Third, AFM may eventually allow the study in real-time of dynamic processes including the assembly, disassembly and conformational rearrangements of virus particles. Fourth, AFM has opened the possibility to investigate previously unexplored physical properties of virus particles, which may provide novel insights into the relationships between virus structure, properties, and functions. Along this line, AFM offers the possibility of probing the mechanical stiffness of virions and capsids and of selectively disrupting elements in individual virus particles (see Chap. 18). These experiments may contribute to understand virus assembly and disassembly, stability and dynamics.

8.6 Perspectives

Some of the current developments in AFM imaging aim to increase the data acquisition speed (a typical AFM image takes a few minutes to be acquired), in order to directly visualize the dynamics of relatively fast biological processes in real time, including conformational changes and the assembly or disassembly of virus particles. For example, AFM imaging at high video rates (80 ms/frame) has been already used to show conformational changes of single myosin V proteins on mica [65]. The methodology to achieve such a high speed AFM involves several technical developments, including the use of very soft cantilevers with a high frequency of resonance in liquids, which is achieved by decreasing the cantilever thickness and reducing the cantilever width and length proportionally.

Mechanical properties of biological objects are generally analyzed in indentation experiments [60]. However, there is also the possibility of using DM operating in liquids to extract information about mechanical properties of virus particles and other biological objects (*e.g.*, their stiffness), by mapping the phase lag [66].

The development of non-invasive AFM imaging techniques where sample destruction is minimized is also important. For example, frequency modulation AFM [67, 68] is a dynamic technique where small forces of a few tens of pN only can be applied to the surface. This promising technique is based on the use of three simultaneous feedbacks. A phase lock loop ensures that the cantilever is always in

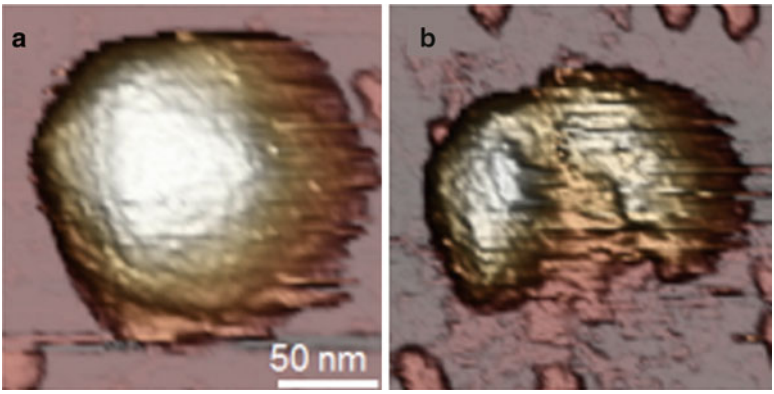

Fig. 8.12 Breaking a virus. (**a**) and (**b**) show a single human adenovirus particle before and after the breakage provoked by pushing the virus with the AFM tip beyond the rupture force in a force vs. z-piezo displacement experiment (Taken from Ref. [69]. Reproduced with permission)

resonance while a second feedback (working over the phase lock loop) changes the tip-sample gap to keep a set point frequency, such that its output gives the topography. Lastly, a third feedback is used to maintain the oscillation amplitude constant by changing the amplitude of the cantilever driving signal, which results in more stable operation.

Finally, it is important to stress the ability of AFM to mechanically manipulate and modify individual virus particles. The first experimental approaches, published very recently, are based upon the application of mechanical stress above the rupture force, thus provoking a rather uncontrolled dismantling of virus particles (Fig. 8.12) [53, 54, 69]. In the future the adequate control of the mechanical stress dosage may unveil further important insights into virus assembly, disassembly and dynamics [1].

In summary, the ongoing developments in AFM promise to improve its applicability in structural virology by: (i) further reducing unwanted sample damage; (ii) increasing the spatial resolution; (iii) increasing the temporal resolution so that relatively fast structural changes in virus particles can be followed in real time.

Acknowledgements I thank my students Aida Llauró-Portell, Alvaro Ortega-Esteban and Mercedes Hernando-Pérez, who are carrying out the hardest part of the work. I also want to thank my collaborators Nuria Verdaguer, Mauricio G. Mateu, José López Carrascosa, David Reguera, Julio Gómez-Herrero and Carmen San Martín. I acknowledge funding by grants from the Ministry of Science and Innovation of Spain, PIB2010US-00233, FIS2011-29493, Consolider CSD2010-00024, Comunidad de Madrid No. S2009/MAT-1467, and FIS2011-16090-E.

References and Further Reading

1. Ortega-Esteban A, Pérez-Berná AJ, Menéndez-Conejero R, Flint SJ, San Martín C, de Pablo PJ (2013) Monitoring dynamics of human adenovirus disassembly induced by mechanical fatigue. Sci Rep 3: 1434
2. Kuznetsov YG, Xiao CA, Sun SY, Raoult D, Rossmann M, McPherson A (2010) Atomic force microscopy investigation of the giant mimivirus. Virology 404:127–137
3. Roos WH, Radtke K, Kniesmeijer E, Geertsema H, Sodeik B, Wuite GJL (2009) Scaffold expulsion and genome packaging trigger stabilization of herpes simplex virus capsids. Proc Natl Acad Sci USA 106:9673–9678
4. Kuznetsov YG, Low A, Fan H, McPherson A (2004) Atomic force microscopy investigation of wild-type Moloney murine leukemia virus particles and virus particles lacking the envelope protein. Virology 323:189–196
5. Carrasco C, Castellanos M, de Pablo PJ, Mateu MG (2008) Manipulation of the mechanical properties of a virus by protein engineering. Proc Natl Acad Sci USA 105:4150–4155
6. Hernando-Pérez M, Pascual E, Carrasco C, Ionel A, Carrascosa JL, de Pablo PJ (2009) Study of the mechanical properties of bacteriophage T7. Biophys J 96(3):422a–423a
7. Binnig G, Rohrer H (1982) Scanning tunneling microscopy. Helv Physica Acta 55:726–735
8. Chen CJ (1993) Introduction to scanning tunneling microscopy. Oxford University Press, Oxford
9. Baro AM, Miranda R et al (1985) Determination of surface topography of biological specimens at high-resolution by scanning tunnelling microscopy. Nature 315:253–254
10. Binnig G, Quate CF, Gerber C (1986) Atomic force microscope. Phys Rev Lett 56:930–933
11. Schmalz G (1929) Uber Glatte und Ebenheit als physikalisches und physiologishes Problem. Verein Deutscher Ingenieure (Oct 12), pp. 1461–1467
12. Meyer G, Amer NM (1988) Novel optical approach to atomic force microscopy. Appl Phys Lett 53:1045–1047
13. Sader JE, Chon JWM, Mulvaney P (1999) Calibration of rectangular atomic force microscope cantilevers. Rev Sci Instrum 70:3967–3969
14. Butt HJ, Jaschke M (1995) Calculation of thermal noise in atomic-force microscopy. Nanotechnology 6:1–7
15. Israelachvili J (2002) Intermolecular and surface forces. Academic Press, London
16. Johnson KL (1985) Contact mechanics. Cambridge University Press, Cambridge
17. Ohnesorge F, Binnig G (1993) True atomic-resolution by atomic force microscopy through repulsive and attractive forces. Science 260:1451–1456
18. Giessibl FJ (1995) Atomic-resolution of the silicon (111)-(7x7) surface by atomic-force microscopy. Science 267:68–71
19. Sugimoto Y, Pou P, Abe M, Jelinek P, Perez R, Morita S, Custance O (2007) Chemical identification of individual surface atoms by atomic force microscopy. Nature 446:64–67
20. Carpick RW, Ogletree DF, Salmeron M (1997) Lateral stiffness: a new nanomechanical measurement for the determination of shear strengths with friction force microscopy. Appl Phys Lett 70:1548–1550
21. Martin Y, Williams CC, Wickramasinghe HK (1987) Atomic force microscope force mapping and profiling on a sub 100-a scale. J Appl Phys 61:4723–4729
22. Garcia R, Perez R (2002) Dynamic atomic force microscopy methods. Surf Sci Rep 47:197–301
23. Legleiter J, Park M, Cusick B, Kowalewski T (2006) Scanning probe acceleration microscopy (SPAM) in fluids: mapping mechanical properties of surfaces at the nanoscale. Proc Natl Acad Sci 103:4813–4818
24. Kuznetsov YG, Malkin AJ, Lucas RW, Plomp M, McPherson A (2001) Imaging of viruses by atomic force microscopy. J Gen Virol 82:2025–2034

25. Miyatani T, Horii M, Rosa A, Fujihira M, Marti O (1997) Mapping of electrical double-layer force between tip and sample surfaces in water with pulsed-force-mode atomic force microscopy. Appl Phys Lett 71:2632–2634
26. de Pablo PJ, Colchero J, Gomez-Herrero J, Baro AM (1998) Jumping mode scanning force microscopy. Appl Phys Lett 73:3300–3302
27. de Pablo PJ, Colchero J, Gomez-Herrero J, Baro AM, Schaefer DM, Howell S, Walsh B, Reifenberger R (1999) Adhesion maps using scanning force microscopy techniques. J Adhes 71:339–356
28. Ortega-Esteban A, Horcas I, Hernando-Pérez M, Ares P, Pérez-Berná AJ, San Martín C, Carrascosa JL, de Pablo PJ, Gómez-Herrero J (2012) Minimizing tip-sample forces in jumping mode atomic force microscopy in liquid. Ultramicroscopy 114:56–61
29. Villarrubia JS (1997) Algorithms for scanned probe microscope image simulation, surface reconstruction, and tip estimation. J Res Natl Inst Stan Technol 102:425–454
30. Marti O, Drake B, Gould S, Hansma PK (1988) Atomic resolution atomic force microscopy of graphite and the native oxide on silicon. J Vac Sci Technol a-Vac Surf Films 6:287–290
31. Soler JM, Baro AM, Garcia N, Rohrer H (1986) Interatomic forces in scanning tunneling microscopy—giant corrugations of the graphite surface. Phys Rev Lett 57:444–447
32. Hansma HG, Sinsheimer RL, Li MQ, Hansma PK (1992) Atomic force microscopy of single-stranded and double-stranded DNA. Nucleic Acids Res 20:3585–3590
33. Lyubchenko YL, Jacobs BL, Lindsay SM, Stasiak A (1995) Atomic-force microscopy of nucleoprotein complexes. Scanning Microscopy 9:705–727
34. Dame RT, Wyman C, Goosen N (2003) Insights into the regulation of transcription by scanning force microscopy. Journal of Microscopy-Oxford 212:244–253
35. Janicijevic A, Ristic D, Wyman C (2003) The molecular machines of DNA repair: scanning force microscopy analysis of their architecture. Journal of Microscopy-Oxford 212:264–272
36. Wagner P, Hegner M, Guntherodt HJ, Semenza G (1995) Formation and in-situ modification of monolayers chemisorbed on ultraflat template-stripped gold surfaces. Langmuir 11:3867–3875
37. Muller DJ, Amrein M, Engel A (1997) Adsorption of biological molecules to a solid support for scanning probe microscopy. J Struct Biol 119:172–188
38. Muller DJ, Janovjak H, Lehto T, Kuerschner L, Anderson K (2002) Observing structure, function and assembly of single proteins by AFM. Prog Biophys Mol Biol 79:1–43
39. Hansma HG, Pietrasanta L (1998) Atomic force microscopy and other scanning probe microscopies. Curr Opin Chem Biol 2:579–584
40. Horber JKH, Miles MJ (2003) Scanning probe evolution in biology. Science 302:1002–1005
41. Hinterdorfer P, Dufrene YF (2006) Detection and localization of single molecular recognition events using atomic force microscopy. Nat Meth 3:347–355
42. Neuman KC, Nagy A (2008) Single-molecule force spectroscopy: optical tweezers, magnetic tweezers and atomic force microscopy. Nat Meth 5:491–505
43. Kirmizis D, Logothetidis S (2010) Atomic force microscopy probing in the measurement of cell mechanics. Int J Nanomed 5:137–145
44. Kurland NE, Drira Z, Yadavalli VK (2012) Measurement of nanomechanical properties of biomolecules using atomic force microscopy. Micron 43:116–128
45. Viani MB, Pietrasanta LI, Thompson JB, Chand A, Gebeshuber IC, Kindt JH, Richter M, Hansma HG, Hansma PK (2000) Probing protein-protein interactions in real time. Nat Struct Biol 7:644–647
46. Moreno-Herrero F, Colchero J, Gomez-Herrero J, Baro AM (2004) Atomic force microscopy contact, tapping, and jumping modes for imaging biological samples in liquids. Phys Rev E 69:031915
47. Xu X, Carrasco C, de Pablo PJ, Gomez-Herrero J, Raman A (2008) Unmasking imaging forces on soft biological samples in liquids when using dynamic atomic force microscopy: a case study on viral capsids. Biophys J 95:2520–2528

48. Kasas S, Thomson NH, Smith BL, Hansma HG, Zhu X, Guthold M, Bustamante C, Kool ET, Kashlev M, Hansma PK (1997) Escherichia coli RNA polymerase activity observed using atomic force microscopy. Biochemistry 36:461–468
49. Moreno-Herrero F, de Jager M, Dekker NH, Kanaar R, Wyman C, Dekker C (2005) Mesoscale conformational changes in the DNA-repair complex Rad50/Mre11/Nbs1 upon binding DNA. Nature 437:440–443
50. Kodera N, Yamamoto D, Ishikawa R, Ando T (2010) Video imaging of walking myosin V by high-speed atomic force microscopy. Nature 468:72–76
51. Plomp M, Rice MK, Wagner EK, McPherson A, Malkin AJ (2002) Rapid visualization at high resolution of pathogens by atomic force microscopy – Structural studies of herpes simplex virus-1. Am J Pathol 160:1959–1966
52. Kuznetsov YG, McPherson A (2011) Atomic force microscopy in imaging of viruses and virus-infected cells. Microbiol Mol Biol Rev 75:268–285
53. Ivanovska IL, Miranda R, Carrascosa JL, Wuite GJL, Schmidt CF (2011) Discrete fracture patterns of virus shells reveal mechanical building blocks. Proc Natl Acad Sci USA 108:12611–12616
54. Castellanos M, Perez R, Carrillo PJP, Pablo PJ, Mateu MG (2012) Mechanical disassembly of single virus particles reveals kinetic intermediates predicted by theory. Biophys J 102:2615–2624
55. Sieben C, Kappel C, Zhu R, Wozniak A, Rankl C, Hinterdorfer P, Grubmüller H, Herrmann A (2012) Influenza virus binds its host cell using multiple dynamic interactions. Proc Natl Acad Sci USA 109:13626–13631
56. Xiao C, Kuznetsov YG, Sun S, Hafenstein SL, Kostyuchenko VA, Chipman PR, Suzan-Monti M, Raoult D, McPherson A, Rossmann MG (2009) Structural studies of the giant mimivirus. PLoS Biol 7:958–966
57. Vinckier A, Heyvaert I, Dhoore A, Mckittrick T, Vanhaesendonck C, Engelborghs Y, Hellemans L (1995) Immobilizing and imaging microtubules by atomic-force microscopy. Ultramicroscopy 57:337–343
58. Carrasco C, Luque A, Hernando-Pérez M, Miranda R, Carrascosa JL, Serena PA, de Ridder M, Raman A, Gómez-Herrero J, Schaap IA, Reguera D, de Pablo PJ (2011) Built-in mechanical stress in viral shells. Biophys J 100:1100–1108
59. Roos WH, Bruinsma R, Wuite GJL (2010) Physical virology. Nat Phys 6:733–743
60. Ivanovska IL, de Pablo PJ, Ibarra B, Sgalari G, MacKintosh FC, Carrascosa JL, Schmidt CF, Wuite GJ (2004) Bacteriophage capsids: Tough nanoshells with complex elastic properties. Proc Natl Acad Sci USA 101:7600–7605
61. Kienberger F, Zhu R, Moser R, Blaas D, Hinterdorfer P (2004) Monitoring RNA release from human rhinovirus by dynamic force microscopy. J Virol 78:3203–3209
62. Tang JH, Olson N, Jardine PJ, Grimes S, Anderson DL, Baker TS (2008) DNA poised for release in bacteriophage phi 29. Structure 16:935–943
63. Horcas I, Fernandez R, Gomez-Rodriguez JM, Colchero J, Gomez-Herrero J, Baro AM (2007) WSXM: A software for scanning probe microscopy and a tool for nanotechnology. Rev Sci Instrum 78:013705
64. Carrasco C, Carreira A, Schaap IAT, Serena PA, Gomez-Herrero J, Mateu MG, de Pablo PJ (2006) DNA-mediated anisotropic mechanical reinforcement of a virus. Proc Natl Acad Sci USA 103:13706–13711
65. Ando T, Kodera N, Takai E, Maruyama D, Saito K, Toda A (2001) A high-speed atomic force microscope for studying biological macromolecules. Proc Natl Acad Sci USA 98:12468–12472
66. Melcher J, Carrasco C, Xu X, Carrascosa JL, Gómez-Herrero J, de Pablo PJ, Raman A (2009) Origins of phase contrast in the atomic forces microscopy in liquids. Proc Nat Acad Sci 106:13655–13660
67. Hoogenboom BW, Hug HJ, Pellmont Y, Martin S, Frederix PLTM, Fotiadis D, Engel A (2006) Quantitative dynamic-mode scanning force microscopy in liquid. Appl Phys Lett 88:193109

68. Martinez-Martin D, Carrasco C, Hernando-Perez M, de Pablo PJ, Gomez-Herrero J, Perez R, Mateu MG, Carrascosa JL, Kiracofe D, Melcher J, Raman A (2012) Resolving structure and mechanical properties at the nanoscale of viruses with frequency modulation atomic force microscopy. PLoS One 7:e30204
69. Pérez-Berná AJ, Ortega-Esteban A, Menéndez-Conejero R, Winkler DC, Menéndez M, Steven AC, Flint SJ, de Pablo PJ, San Martín C (2012) The role of capsid maturation on adenovirus priming for sequential uncoating. J Biol Chem 287:31582–31595

Further Reading

Samorí P (ed) (2006) Scanning force microscopies beyond imaging. Wiley-VCH Weinheim, Germany
Baró A, Reifenberger R (2012) Atomic force microscopy in liquid. Wiley-VCH Weinheim, Germany

Also especially recommended for further reading are references [3, 4, 7, 21, 22, 45, 49] *listed above*.